*Sensors and Materials*, Vol. 37, No. 4 (2025) 1503–1525
MYU Tokyo


S & M 4001

# Improving the Performance of Deformation Monitoring for Large-scale Power Infrastructure Using Multifrequency Global Navigation Satellite System Observations

Jiaxing Wang, Gen Liu,* Haochen Guo, Nanjun Ma, and Jian Wang

School of Geomatics and Urban Spatial Informatics, Beijing University of Civil Engineering and Architecture,
15 Yongyuan Road, Daxing, Beijing 102616, China

(Received January 23, 2025; accepted March 31, 2025)

***Keywords:*** multifrequency GNSS, deformation monitoring, large-scale power infrastructure, signal quality assessment, static baseline positioning

With the rapid development of high-voltage transmission lines in China, traditional deformation monitoring technologies face challenges such as limited accuracy and poor adaptability to complex environments. These limitations become particularly evident in regions with complex terrain or severe weather conditions. To address these challenges, we introduce multifrequency Global Navigation Satellite System (GNSS) technology as a solution to enhance both the accuracy and efficiency of deformation monitoring for large-scale power infrastructure, especially high-voltage transmission line towers. We implement multifrequency GNSS technology for the long-term, all-weather monitoring of transmission line tower deformations. By integrating GNSS data quality analysis, we propose a customized monitoring solution tailored for large-scale power infrastructure. To evaluate the effectiveness of multifrequency GNSS, a comparative analysis is conducted against traditional dual-frequency GNSS technology, and the improvements in positioning accuracy and reliability are assessed. The results demonstrate that multifrequency GNSS significantly enhances the deformation monitoring precision. In particular, BDS triple-frequency solutions improve accuracy by 40.57, 44.5, and 36.8% in the E, N, and U directions, respectively, compared with dual-frequency solutions. Similarly, GPS triple-frequency solutions achieve improvements of 43.29, 43.45, and 37.2%. Moreover, both BDS and GPS triple-frequency solutions achieve a positioning accuracy of 3 mm in the horizontal direction and 5 mm in the vertical direction, maintaining stable performance over multiple days. These findings underscore the significant practical advantages of multifrequency GNSS in ensuring high-precision deformation monitoring for large-scale power infrastructure.

*Corresponding author: e-mail: liugen@bucea.edu.cn
https://doi.org/10.18494/SAM5554

ISSN 0914-4935 

## 1. Introduction

By the end of 2024, China had established approximately 194 inter-regional AC transmission lines of 330 kV and above, with a total length of about 34843 km, as well as 43 direct current transmission lines spanning approximately 55900 km. These extensive transmission lines are supported by a vast network of large-scale infrastructure, which forms the backbone of the power system. This infrastructure ensures stable and efficient energy transmission, promotes regional interconnectivity, and enhances the reliability and safety of electricity supply. However, long-distance transmission lines often traverse environmentally complex regions, such as mountains, rivers, and deserts. Transmission towers in these areas are particularly susceptible to deformation caused by geological activity and extreme weather conditions, posing risks to the stable and safe operation of the power grid. Subtle and gradual deformations, which are difficult to detect, necessitate high-precision, long-term monitoring to identify potential risks and prevent failures. Traditional monitoring methods, such as manual inspections, frequently fail to address these challenges effectively. These methods are often limited by subjectivity, low inspection frequency, and restricted coverage, making it difficult to capture early signs of deformation. Consequently, their ability to prevent risks is inadequate, leaving significant gaps in the monitoring and maintenance of large-scale power infrastructure. Therefore, improving the performance of deformation monitoring is of critical importance to ensure the safe and reliable operation of large-scale power infrastructure.(1,2)

The Global Navigation Satellite System (GNSS) and corresponding positioning sensors, known for their continuous, real-time, high-precision, and all-weather measurement capabilities, has been extensively applied in the deformation monitoring of large-scale infrastructure in recent years.(3,4) In 1993, Lovse *et al.* demonstrated the feasibility of using GPS for the dynamic deformation monitoring of bridges, towers, and high-rise buildings. Using the Calgary Tower as a case study, they conducted differential GPS measurements and identified its vibration frequency under wind loads to be approximately 0.3 Hz, with an east–west amplitude of 5 mm and a north–south amplitude of 15 mm.(5) In 2002, Breuer *et al.* utilized GPS technology to monitor the dynamic response of the 150-m-high Stuttgart TV Tower in Germany under light wind loads. They also analyzed its quasi-static deformation characteristics caused by variations in sunlight and temperature through static GPS observations.(6) In 2005, Guo *et al.* introduced the capabilities of a GPS-RTK (Real Time Kinematic) real-time bridge monitoring system. Using the Humen Bridge as an example, they analyzed the effects of temperature on deck deformation and vibration frequency, showing that GPS-RTK results were highly consistent with those of finite element analysis.(7) In 2007, Dai *et al.* developed GPS Dynamic Deformation Monitoring Software using C++ and validated its effectiveness through the experimental monitoring of high-rise residential buildings.(8) In 2021,Vázquez-Ontiveros *et al.* employed GPS observations to investigate the relationship between gravity dam deformation and reservoir water level changes, confirming the utility of GPS in monitoring hydraulic infrastructure.(9) More recently, in 2022, Shen *et al.* proposed an Interacting Multiple Model (IMM) method based on high-frequency GNSS, significantly enhancing the accuracy and resolution of vertical vibration monitoring.(10) The results of these extensive studies have consistently validated the feasibility of GNSS in monitoring the deformation of large-scale infrastructure. Given that large-scale power infrastructure falls under this category, achieving millimeter-level precision in their monitoring is crucial. However, the operational environment around most large-scale power infrastructure presents considerable challenges. For instance, the high-voltage currents near transmission lines generate strong electromagnetic interference, which can disrupt the normal operation of GNSS receivers, causing signal instability and increased measurement errors. In addition to electromagnetic interference, factors such as complex geographic conditions, obstructions from surrounding buildings, and weather variability further degrade measurement accuracy.(11) These environmental challenges collectively contribute to reduced monitoring precision in the deformation monitoring of large-scale power infrastructure.

With the advent of multifrequency and multisystem GNSS technology, positioning accuracy and stability have been significantly enhanced.(12) Unlike dual-frequency GNSS, multifrequency GNSS capitalizes on signals from multiple frequency bands and offers marked advantages in measurement precision. Liu analyzed the relative positioning models of BDS dual-frequency and triple-frequency systems and found that the B1/B2/B3 triple-frequency combination significantly improves relative positioning accuracy compared with the dual-frequency configuration.(13) Similarly, Yang examined the positioning accuracy of GPS triple-frequency and dual-frequency systems in short baseline relative positioning and found that the triple-frequency combination consistently outperforms both dual-frequency and single-frequency configurations in terms of positioning precision.(14) Furthermore, Zhang investigated the RTK performance of BDS dual-frequency and triple-frequency systems across various baseline lengths and revealed that while the positioning accuracy of both systems decreased with increasing baseline length, the triple-frequency combination consistently demonstrated superior accuracy over the dual-frequency configuration.(15) In conclusion, by leveraging signals from multiple frequency bands, multifrequency GNSS effectively reduces the impact of ionospheric delays and multipath effects, thus significantly enhancing signal quality and positioning stability. This becomes particularly advantageous in environments near large-scale power infrastructure, where electromagnetic interference and signal blockages present considerable challenges to traditional GNSS systems. Owing to its signal redundancy and superior anti-interference capabilities, multifrequency GNSS offers a more reliable means of signal reception. However, despite its potential, research into the practical enhancement of multifrequency GNSS data for deformation monitoring in the real-world settings of large-scale power infrastructure remains limited and further investigation is warranted.

We further explore the practical effectiveness of multifrequency GNSS data in the deformation monitoring of large-scale power infrastructure, focusing particularly on its impact on data quality and improvements in complex environments. Additionally, we critically examine the feasibility and advantages of using multifrequency GNSS for long-term, high-precision monitoring.

The structure of this paper is as follows. First, the introduction outlines the significance of deformation monitoring for large-scale power infrastructure, emphasizing the potential of multifrequency GNSS in complex environments and the unresolved challenges that remain. In the methodology section, we provide a comprehensive description of the indicators used for

GNSS data quality assessment—such as data completeness, signal-to-noise ratio (*SNR*), cycle slip ratio (*CSR*), and multipath error,—and the corresponding calculation methods, along with the development of multifrequency GNSS positioning models (including both functional and stochastic models). The deformation monitoring method is also discussed, detailing the approach used to monitor and analyze the deformation of large-scale power infrastructure. In the experimental analysis and discussion section, we assess the advantages of multifrequency data with respect to data quality, positioning precision, and monitoring stability on the basis of an analysis of static baseline observation data collected under complex electromagnetic conditions, and compare these results with those of dual-frequency systems. Finally, in the conclusion and outlook section, we summarize the superior performance of multifrequency GNSS in the deformation monitoring of large-scale power infrastructure and provide research recommendations for future studies, including anti-jamming algorithms, multisource data fusion, and predictive modeling.

## 2. Methods

### 2.1 GNSS data quality assessment

In the deformation monitoring of large-scale power infrastructure, the primary GNSS data quality assessment indicators include data completeness, *SNR*, *CSR*, and multipath error. Data completeness ensures the continuity of observation data, maintaining the integrity of the monitoring time series. The *SNR* is a measure of the quality of the signals, allowing for the elimination of low-quality data affected by interference or obstruction. The *CSR* helps detect signal discontinuities, minimizing the propagation of errors. Multipath error analysis identifies and removes data affected by reflected signals. A comprehensive evaluation of these indicators enhances both the monitoring accuracy and the system's resistance to interference, thereby supporting efficient positioning and enabling long-term trend analysis.

#### 2.1.1 Data completeness

Data completeness refers to the ratio of the actual number of epochs of satellite observations recorded by the receiver to the theoretical number of epochs, and is used to assess the continuity and quality of the observation data.[16] A higher data completeness indicates a higher data quality. The data completeness indicator is extracted through the following formula:

$$DI_f = \left( \frac{\sum_{j=1}^{n} A^j}{\sum_{j=1}^{n} B^j} \right) \times 100\%, \tag{1}$$

where $DI_f$ represents the data completeness rate; $n$ is the total number of observed satellites; $A^j$ is the total number of actual observation epochs for the $j$ satellite at a specific frequency during the observation period; and $B^j$ is the total number of theoretical observation epochs for the $i$ satellite at the specific frequency during the observation period.

In the monitoring environment of large-scale power infrastructure, complex factors such as electromagnetic interference and signal obstructions can cause data loss, impacting monitoring accuracy and reliability. To ensure the effective detection of subtle structural deformations and prevent false alarms in critical regions—such as high-voltage towers in mountainous or densely populated urban areas—the data completeness rate must be maintained at a minimum of 90%.(17)

### 2.1.2 *SNR*

The *SNR* is the ratio of the received carrier signal power to the noise power. It is primarily affected by the gain at both the satellite transmission end and the receiver end. The *SNR* reflects the quality of the satellite signal and the performance of the receiver; a higher *SNR* indicates a higher signal quality.(18) Its calculation formula is

$$SNR = 10 \cdot \log_{10}\left(\frac{P_{signal}}{P_{noise}}\right), \tag{2}$$

where $P_{signal}$ represents the signal power and $P_{noise}$ the noise power.

In the deformation monitoring of large-scale power infrastructure, strong electromagnetic interference and signal obstructions near transmission towers can degrade the signal quality, leading to increased positioning errors and reduced monitoring reliability. To ensure stable and high-precision deformation monitoring, an average *SNR* of at least 35–40 dB-Hz is required.(19) A lower *SNR* may result in unstable carrier phase tracking, higher cycle slip occurrence, and degraded positioning accuracy, particularly in environments with severe electromagnetic disturbances or dense structural obstructions.

### 2.1.3 *CSR*

Cycle slip refers to the phenomenon in which satellite signals lose lock and subsequently reacquire it owing to obstructions caused by surrounding buildings, vegetation, or terrain near the observation station. This results in a jump in the integer cycle count of the carrier phase measurements, reflecting the quality of the environment around the observation station.(20)

To assess the occurrence of cycle slips in the observation data, the *CSR* is introduced, defined as

$$CSR = \frac{1000}{O / slips}, \tag{3}$$

where the ratio *O/slips* represents the number of cycle slips relative to the total number of observation epochs. A smaller *CSR* value indicates fewer cycle slips and a higher data quality.(21)

For the deformation monitoring of large-scale power infrastructure, the *CSR* should be maintained below 5 to ensure stable and reliable observation data.(22) Excessive cycle slips can disrupt phase continuity, introduce large positioning errors, and compromise long-term deformation trend analysis. This is particularly critical in high-voltage transmission environments where frequent electromagnetic interference and signal obstructions increase the likelihood of cycle slips, affecting the accuracy and consistency of monitoring results.

### 2.1.4 Multipath error

Multipath error typically reflects the impact of the surrounding environment and other factors on signal propagation. The smaller the multipath error, the higher the resistance to multipath interference.(23) Multipath error extraction techniques are typically based on the combination of pseudorange and carrier phase measurements. These errors can be extracted using

$$MP_{k_1} = \rho_{k_1} - \frac{f_{k_1}^2 + f_{k_2}^2}{f_{k_1}^2 - f_{k_2}^2}\varphi_{k_1} + \frac{2f_{k_2}^2}{f_{k_1}^2 - f_{k_2}^2}\varphi_{k_2} f_{k_1} f_{k_2}, \tag{4}$$

$$MP_{k_2} = \rho_{k_2} - \frac{2f_{k_1}^2}{f_{k_1}^2 - f_{k_2}^2}\varphi_{k_1} + \frac{f_{k_1}^2 + f_{k_2}^2}{f_{k_1}^2 - f_{k_2}^2}\varphi_{k_2}, \tag{5}$$

where $MP_{k_1}$ represents the computational quantity that includes multipath error and integer ambiguity information at frequency $k_1$; $\rho_{k_1}$ is the pseudorange observation at frequency $k_1$; $f_{k_1}$ is the frequency of the navigation signal's carrier at frequency $k_1$; $f_{k_2}$ is the frequency of the navigation signal's carrier at frequency $k_2$; $\varphi_{k_1}$ is the carrier phase observation at frequency $k_1$; $\varphi_{k_2}$ is the carrier phase observation at frequency $k_2$; $MP_{k_2}$ represents the computational quantity that includes multipath errors and integer ambiguity information at frequency $k_2$ and the corresponding number of online devices; and $\rho_{k_2}$ is the pseudorange observation at frequency $k_2$.

For the same satellite observed continuously without cycle slips, the combined ambiguity parameters will remain unchanged. The multipath error indicator is extracted between multiple epochs without cycle slips using

$$\overline{MP_k} = \sqrt{\frac{1}{N_{SW} - 1}\sum_{i=1}^{N_{SW}}\left(MP_k(t_i) - \frac{\sum_{i=1}^{N_{SW}} MP_k(t_i)}{N_{SW}}\right)^2}, \tag{6}$$

where $\overline{MP_k}$ represents the multipath error evaluation value for the satellite observed by the receiver at frequency $k$; $N_{sw}$ is the number of epochs in the sliding window; and $MP_k(t_i)$ is the computational quantity for the multipath error and integer ambiguity information of the satellite observed by the receiver at frequency $k$ at epoch $t_i$.

For the deformation monitoring of large-scale power infrastructure, the multipath error should be kept below 0.5 m to ensure reliable monitoring data and accurate positioning.(24) Excessive multipath interference can distort GNSS signals, leading to positioning errors and reduced monitoring reliability, especially in environments with a large number of transmission towers or reflective surfaces.

## 2.2 Multifrequency GNSS positioning model

In GNSS positioning for the deformation monitoring of large-scale power infrastructure, the processing of observation data is critical to achieving high-precision monitoring. To comprehensively address and resolve positioning issues, it is essential to model the mathematical relationships and stochastic characteristics of the observations. In this process, the models are divided into two categories: functional models and stochastic models. These models complement each other, forming the theoretical foundation of GNSS positioning in the deformation monitoring of large-scale power infrastructure.

### 2.2.1 Functional model

The functional model is the core of GNSS deformation monitoring for large-scale power infrastructure and is used to describe the mathematical relationship between observations and unknown parameters. Carrier phase, with its high-precision characteristics, serves as a fundamental basis for precise positioning. To minimize the impact of errors, carrier phase observation equations typically employ differential processing, including single-difference and double-difference models. These will be introduced separately in the following sections.

In GNSS measurements, the carrier phase observation equation is the key to achieving high-precision positioning. Let $r$ represent the receiver and $s$ represent the satellite, then the carrier phase observation equation at frequency $f$ can be expressed as(25)

$$\Phi_{r,s}^{f} = \rho_{r,s} + c(\delta t_r - \delta t_s) - I_{r,s}^{f} + T_{r,s} + N^{f}\lambda_f + \varepsilon_{\Phi}^{f}, \tag{7}$$

where $\rho_{r,s}$ is the geometric distance between the receiver $r$ and the satellite $s$; $c(\delta t_r - \delta t_s)$ represents the clock difference between the receiver and the satellite; $I_{r,s}^{f}$ is the ionospheric delay, which depends on frequency $f$; $T_{r,s}$ is the tropospheric delay; $N^f$ is the carrier phase ambiguity; $\lambda_f$ is the carrier wavelength for frequency $f$; and $\varepsilon_{\Phi}^{f}$ is the observation noise.

The single-difference model is used to differentiate the observations of the same receiver $r$ for two satellites, $s$ and $k$, in order to eliminate the receiver clock bias $\delta t_r$. It is defined as(26)

$$\Delta\Phi_{r,s,k}^{f} = \Phi_{r,s}^{f} - \Phi_{r,k}^{f}. \tag{8}$$

Substituting the carrier phase observation Eq. (7) into Eq. (8) yields the single-difference equation:

$$\Delta\Phi_{r,s,k}^{f} = \Delta\mathcal{R}_{r,s,k}^{f} + \Delta\mathcal{C}_{k,s}^{f} - \Delta\mathcal{I}_{r,s,k}^{f} + \Delta\mathcal{T}_{r,s,k}^{f} + \Delta N^{f}\lambda_{f} + \Delta\varepsilon_{\Phi}^{f}. \tag{9}$$

Here, $\Delta\Phi_{r,s,k}^{f}$ is the single-difference carrier phase observation value; $\Delta\mathcal{R}_{r,s,k}^{f}$ is the geometric distance difference between the two satellites; $\Delta\mathcal{C}_{k,s}^{f}$ is the clock bias difference between the two satellites; $\Delta\mathcal{I}_{r,s,k}^{f}$ is the ionospheric delay difference; $\Delta\mathcal{T}_{r,s,k}^{f}$ is the tropospheric delay error; $\Delta N^{f}$ is the ambiguity single difference; and $\Delta\varepsilon_{\Phi}^{f}$ is the observation noise single difference.

The double-difference model is built upon the single-difference model, where the single-difference observations from two receivers $r$ and $p$ are further differenced to eliminate the satellite clock bias. The mathematical expression is given as[27–29]

$$\nabla\Delta\Phi_{r,p,s,k}^{f} = \left(\Delta\Phi_{r,s,k}^{f}\right) - \left(\Delta\Phi_{p,s,k}^{f}\right). \tag{10}$$

Upon expansion, the double-difference equation becomes

$$\nabla\Delta\Phi_{r,p,s,k}^{f} = \nabla\Delta\mathcal{R}_{r,p,s,k}^{f} - \nabla\Delta\mathcal{I}_{r,p,s,k}^{f} + \nabla\Delta\mathcal{T}_{r,p,s,k}^{f} + \nabla\Delta N^{f}\lambda_{f} + \nabla\Delta\varepsilon_{\Phi}^{f}, \tag{11}$$

where $\nabla\Delta\Phi_{r,p,s,k}^{f}$ is the double-difference carrier phase observation value; $\nabla\Delta\mathcal{R}_{r,p,s,k}^{f}$ is the geometric distance double difference; $\nabla\Delta\mathcal{I}_{r,p,s,k}^{f}$ is the ionospheric delay double difference; $\nabla\Delta\mathcal{T}_{r,p,s,k}^{f}$ is the tropospheric delay error double difference; $\nabla\Delta N^{f}$ is the ambiguity double difference; and $\nabla\Delta\varepsilon_{\Phi}^{f}$ is the observation noise double difference.

The double-difference model performs differencing on the observation values from two receivers, effectively eliminating the receiver and satellite clock biases. However, in the case of large-scale transmission infrastructure in complex environments, ionospheric and tropospheric errors still have a significant impact on positioning accuracy. To further improve error elimination capabilities and ambiguity resolution efficiency, we introduce three observation frequencies $f_1$, $f_2$, and $f_3$ and optimize the positioning solution using the redundant information from multifrequency observations. Multifrequency observations can enhance error elimination capabilities to some extent, reduce the search space for ambiguity resolution, and improve solution efficiency. The extended double-difference model not only inherits the error elimination capabilities of the traditional model, but also utilizes information from more observation frequencies to optimize the solution process. The mathematical expression of the extended three-frequency double-difference model is as below. For each observation frequency, double differencing is performed separately, and the double-difference equations are

$$\begin{cases} \nabla\Delta\Phi_{r,p,s,k}^{f_1} = (\Phi_{r,s}^{f_1} - \Phi_{r,k}^{f_1}) - (\Phi_{p,s}^{f_1} - \Phi_{p,k}^{f_1}), \\ \nabla\Delta\Phi_{r,p,s,k}^{f_2} = (\Phi_{r,s}^{f_2} - \Phi_{r,k}^{f_2}) - (\Phi_{p,s}^{f_2} - \Phi_{p,k}^{f_2}), \\ \nabla\Delta\Phi_{r,p,s,k}^{f_3} = (\Phi_{r,s}^{f_3} - \Phi_{r,k}^{f_3}) - (\Phi_{p,s}^{f_3} - \Phi_{p,k}^{f_3}). \end{cases} \tag{12}$$

Substituting the carrier phase observation equation, we expand it as follows:

$$\begin{cases} \nabla\Delta\Phi_{r,p,s,k}^{f_1} = \nabla\Delta\mathcal{R}_{r,p,s,k}^{f_1} - \nabla\Delta\mathcal{I}_{r,p,s,k}^{f_1} + \nabla\Delta\mathcal{T}_{r,p,s,k}^{f_1} + \nabla\Delta N^{f_1}\lambda_1 + \nabla\Delta\varepsilon_{\Phi}^{f_1}, \\ \nabla\Delta\Phi_{r,p,s,k}^{f_2} = \nabla\Delta\mathcal{R}_{r,p,s,k}^{f_2} - \nabla\Delta\mathcal{I}_{r,p,s,k}^{f_2} + \nabla\Delta\mathcal{T}_{r,p,s,k}^{f_2} + \nabla\Delta N^{f_2}\lambda_2 + \nabla\Delta\varepsilon_{\Phi}^{f_2}, \\ \nabla\Delta\Phi_{r,p,s,k}^{f_3} = \nabla\Delta\mathcal{R}_{r,p,s,k}^{f_3} - \nabla\Delta\mathcal{I}_{r,p,s,k}^{f_3} + \nabla\Delta\mathcal{T}_{r,p,s,k}^{f_3} + \nabla\Delta N^{f_3}\lambda_3 + \nabla\Delta\varepsilon_{\Phi}^{f_3}. \end{cases} \tag{13}$$

In the short-baseline scenario, ionospheric and tropospheric delays can be completely eliminated, and the simplified double-difference equation becomes

$$\begin{cases} \nabla\Delta\Phi_{r,p,s,k}^{f_1} = \nabla\Delta\mathcal{R}_{r,p,s,k}^{f_1} + \nabla\Delta N^{f_1}\lambda_1 + \nabla\Delta\varepsilon_{\Phi}^{f_1}, \\ \nabla\Delta\Phi_{r,p,s,k}^{f_2} = \nabla\Delta\mathcal{R}_{r,p,s,k}^{f_2} + \nabla\Delta N^{f_2}\lambda_2 + \nabla\Delta\varepsilon_{\Phi}^{f_2}, \\ \nabla\Delta\Phi_{r,p,s,k}^{f_3} = \nabla\Delta\mathcal{R}_{r,p,s,k}^{f_3} + \nabla\Delta N^{f_3}\lambda_3 + \nabla\Delta\varepsilon_{\Phi}^{f_3}. \end{cases} \tag{14}$$

From the above equation, we can clearly see that the three-frequency double-difference model efficiently eliminates ionospheric errors by incorporating observations from three frequencies. It provides higher redundancy and adapts to multipath effects, signal obstructions, and noisy environments.

### 2.2.2 Stochastic model

The stochastic model directly affects the weight distribution of multifrequency GNSS observation data and the accuracy of positioning results, making it a key factor in the quality of the solution. When processing multifrequency GNSS raw observations for large-scale power infrastructure monitoring, different prior assumptions lead to the generation of distinct weight matrices, resulting in variations in solution outcomes. Therefore, the estimation and precision of unknown parameters are highly dependent on the stochastic model used. In this study, for large-scale power infrastructure monitoring, we adopt the elevation-angle- and *SNR*-based stochastic models.

The elevation-angle-based stochastic model is a weight distribution model established on the basis of the relationship between the satellite elevation angle and GNSS observation errors. As the satellite-elevation angle decreases, its signal becomes more susceptible to atmospheric refraction errors (such as tropospheric and ionospheric errors) and multipath effects, resulting in fluctuations in the accuracy of the observation values. To address this, the model adjusts the observation value weights using mathematical functions to reduce the error impact from low-elevation satellites. Commonly used weight calculation methods include sine- and cosine-based models, expressed as[30,31]

$$\sigma_i^2 = \frac{1}{\sin^2(E(i))} \text{ or } \sigma_i^2 = \frac{1}{\cos^2(E(i))}. \tag{15}$$

In this equation, $E(i)$ represents the elevation angle of the satellite at the $i$ moment. Through this approach, the model can effectively improve the accuracy and reliability of the positioning solution results. Particularly for the large-scale transmission infrastructure discussed in this paper, this model reduces the weight of low-elevation-angle signals, effectively minimizing the impact of electromagnetic interference and multipath effects on the monitoring results. This in turn improves the accuracy of the positioning solution and the reliability of the monitoring data.

The *SNR* is the ratio of signal strength to noise strength at a specific moment and is used to reflect the quality of the observations. Factors affecting the *SNR* include hardware-related factors (such as antenna and receiver types) and environmental factors (such as multipath effects). The *SNR* is typically proportional to the quality of the observation values, while the impact of multipath effects on the *SNR* is inversely related. On the basis of this relationship, the weight of the *SNR* stochastic model can be expressed as[32]

$$\sigma_i^2 = \frac{1}{SNR_i}. \tag{16}$$

The *SNR* stochastic model dynamically adjusts the weights to effectively enhance the reliability of observation data around large-scale power infrastructure. Particularly in environments with signal obstructions or electromagnetic interference, higher weights are assigned to high *SNR* data, which helps reduce the impact of low-quality data on positioning.

### 2.3 Deformation monitoring methods

The deformation monitoring method in this study is illustrated in Fig. 1 and includes the layout of reference and mobile stations, data collection, data preprocessing, data quality analysis, the GNSS static baseline solution, and the conversion of deformation parameters. Data are collected using GNSS equipment, followed by preprocessing and quality analysis to ensure accuracy and reliability. The GNSS static baseline solution is then used to calculate the deformation parameters between the reference and mobile stations, which are compared with preset thresholds (horizontal and vertical displacement thresholds of ±8 and ±10 mm, respectively). If the deformation parameters exceed the thresholds, the early warning system is triggered, enabling prompt response to potential risks. If the thresholds are not exceeded, routine monitoring continues, completing the closed-loop monitoring process. The entire system enables real-time deformation monitoring and early warning, demonstrating high efficiency and reliability.

## 3. Experimental Analysis and Discussion

### 3.1 Experimental strategy and monitoring system

To verify whether multifrequency data can improve the monitoring performance of deformation in large-scale power infrastructure, we selected the observation station data from

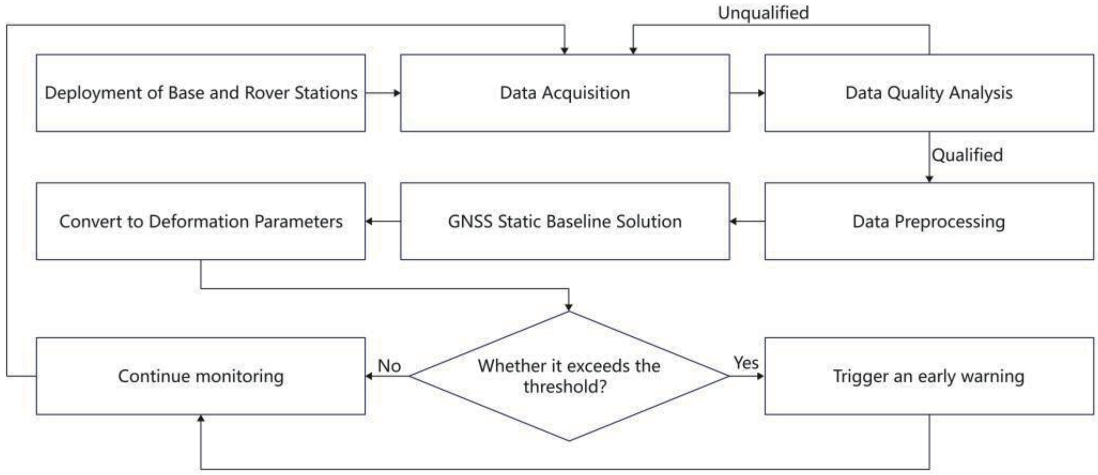


Fig. 1. Deformation monitoring process.

April 11 to 13, 2024, at a large transmission tower at Chaka Salt Lake, Qinghai Province, China, for analysis. The work site and the monitoring reference station layout are shown in Fig. 2. The sites include one reference station (YHJZ) and four monitoring stations (YHJA, YHJB, YHJC, and YHJD). The monitoring stations are located on four large transmission towers, with the reference station approximately 4 km away from the monitoring points. Figure 3 shows the GNSS monitoring equipment installed on the large-scale transmission towers at monitoring stations A and B.

The main challenges in this setup include strong electromagnetic interference from transmission lines, which affects GNSS signal stability, and harsh environmental conditions, such as extreme temperature fluctuations and high-altitude winds, complicating equipment installation and maintenance.

The static baseline processing strategy is summarized in Table 1. For the study area, a static relative positioning mode is employed with a time interval of 30 s. The multifrequency observation data from BDS, GPS, and Galileo are processed using the double-difference model. A 15° elevation angle is set to reduce the error impact of low-elevation signals. Forward filtering is used to achieve an efficient convergence of baseline solutions, and broadcast ephemeris and clock bias data are incorporated to meet real-time requirements. The short-baseline solution significantly reduces ionospheric and tropospheric errors using the double-difference model and ensures the stability of the solution by continuously fixing the integer ambiguities.

Using multifrequency GNSS data and high-precision processing, we developed a deformation monitoring system for large-scale transmission infrastructure (Fig. 4). The system includes GNSS monitoring equipment, a 4G transmission module, a solar-powered unit, and a cloud-based data platform. GNSS collects deformation data, transmits them in real time via 4G, and visualizes them through monitoring software for remote management and safety assessment.

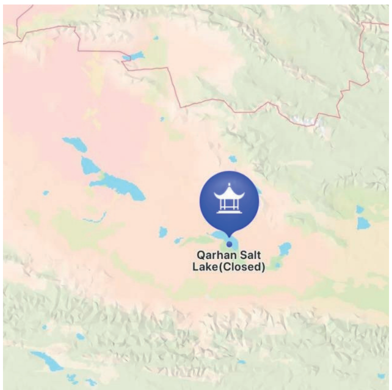


(a)

(b)

Fig. 2. (Color online) (a) Work site and (b) monitoring reference station.

(a)

(b)

Fig. 3. (Color online) Monitoring stations (a) A and (b) B of large-scale transmission towers.

Table 1
Static baseline processing strategy.

| Item | Strategy |
|---|---|
| Position mode | Static |
| Interval | 30 s |
| Frequencies | BDS: B1/B2/B3; Galileo: E1/E5b/E5a; GPS: L1/L2/L5 |
| Filter type | Forward |
| Elevation mask | 15° |
| Observation weight | Elevation-dependent weight |
| RecDynamics | OFF |
| Earth tide correction | OFF |
| Satellite ephemeris/clock | Broadcast |
| Satellite system | BDS-2/GPS/Galileo |
| Integer ambiguity res | Continuous |

### 3.2 Multifrequency GNSS data quality analysis

For the monitoring data, we first evaluated the data quality in an electromagnetic interference environment. We calculated the data completeness rate, *SNR*, *CSR*, and multipath error for a

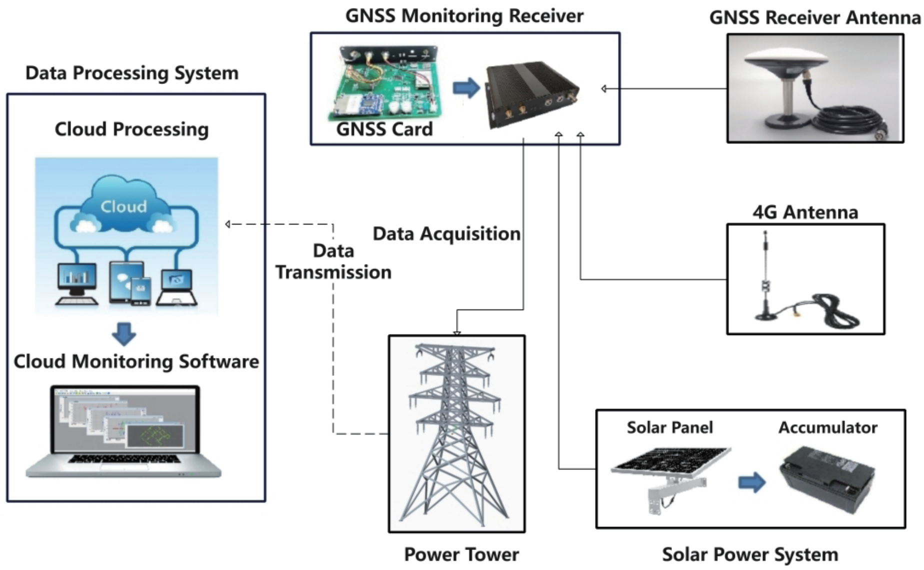


Fig. 4. (Color online) Deformation monitoring system for large-scale power infrastructure.

reference station and four monitoring stations across nine frequencies from three systems: BDS (B1/B2/B3), Galileo (E1/E5b/E5a), and GPS (L1/L2/L5).

### 3.2.1 Data completeness rate analysis

Figure 5 shows the data completeness rate for each frequency of BDS, Galileo, and GPS. As shown, at the reference station YHJZ, the data completeness rate for all frequencies exceeds 90%, with BDS frequencies reaching values above 97%. At the four monitoring stations, the data completeness rate for BDS frequencies remains above 90%, and the completeness rate for GPS L1 and L2 frequencies also exceeds 90%. The L5 frequency has a slightly lower completeness rate but still remains above 85%. However, the data completeness rate for all frequencies of Galileo is generally lower, ranging from 60 to 80%, with the completeness rate for each frequency at monitoring station YHJC being only 30.03, 28.49, and 27.54%, which are significantly lower than those of other systems. We believe that the electromagnetic interference from the transmission tower and other factors have affected all frequencies, with the Galileo system's signal reception being particularly impacted.

### 3.2.2 *SNR* analysis

The comparison of *SNR* between BDS, GPS, and Galileo at each frequency is shown in Fig. 6. From the results, it can be observed that the *SNR* for all frequencies at both the reference station and the four monitoring stations exceeds 35 dB-Hz. Compared with the reference station, the *SNR*s at the monitoring stations generally decreased across all frequencies. For BDS, the *SNR*s at all frequencies exceed 42 dB-Hz; for GPS, all frequencies except L2, which is around 37

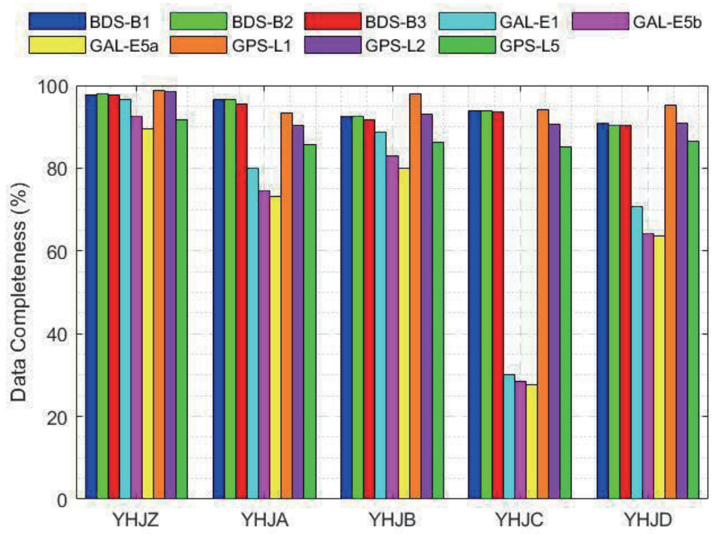


Fig. 5. (Color online) BDS/Galileo/GPS frequency bands.

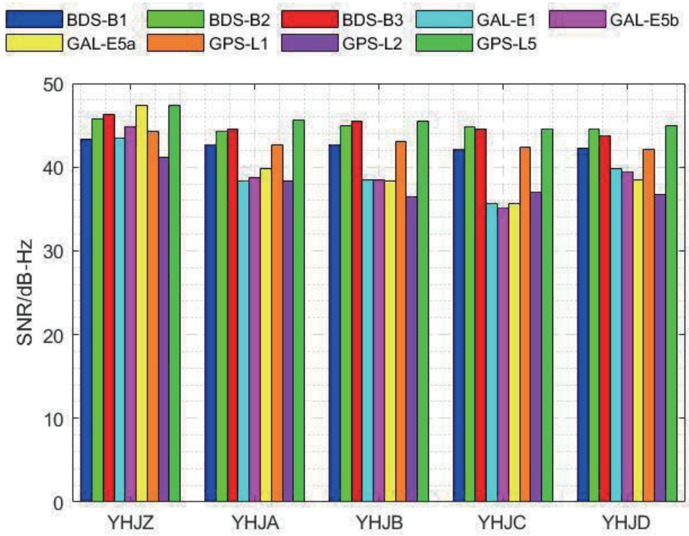


Fig. 6. (Color online) *SNRs* of BDS/Galileo/GPS frequency bands.

dB-Hz, also exceed 42 dB-Hz. For Galileo, the *SNR* at YHJC monitoring station is around 35 dB-Hz, while those at other monitoring stations range between 38 and 42 dB-Hz. However, the *SNR* of Galileo is still lower than those of BDS-2 and GPS.

### 3.2.3 *CSR* analysis

Figure 7 shows the *CSR* for each frequency of BDS, GPS, and Galileo. At the reference station, *CSR* for all frequencies remains below 5, with BDS exhibiting the lowest values, generally below 1. The Galileo system's *CSR* ranges from 1 to 2, while GPS shows higher values

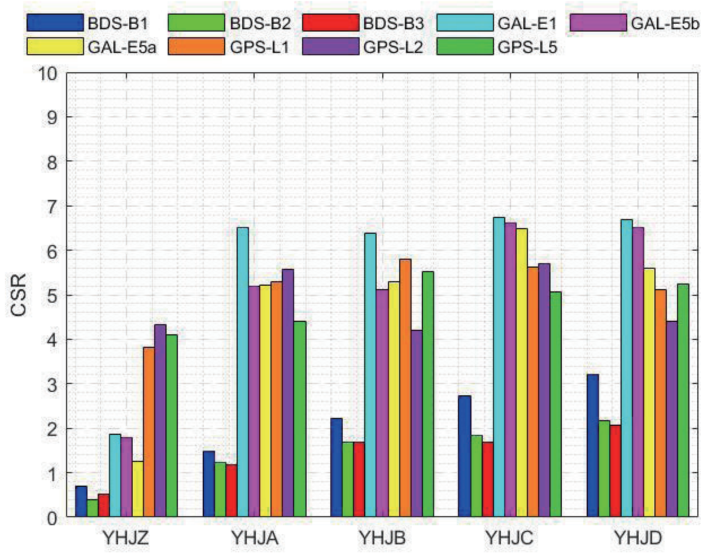


Fig. 7. (Color online) *CSR*s of BDS/Galileo/GPS frequency bands.

between 3.5 and 4.5. At the monitoring stations, the *CSR* increases across all frequencies. BDS maintains stability with values between 1 and 3, and those of GPS range from 4 to 6 with some frequencies slightly exceeding 5. The *CSR* of Galileo rises significantly to 5–7, the highest among the three systems. Overall, BDS demonstrates the best performance, consistently meeting the *CSR* requirement below 5. While some GPS frequencies exceed this threshold, GPS still outperforms Galileo, which has *CSR* values above 5 across all frequencies.

#### 3.2.4 Multipath error analysis

Figure 8 shows the average multipath error (unit: cm) for each frequency of BDS, Galileo, and GPS. The results indicate that in the reference station environment, the multipath error for all frequencies of each system is below 50 cm, with BDS exhibiting the lowest multipath error that remains stable between 12 and 20 cm, which is the best among the three systems. Compared with the reference station, the multipath error increases at the monitoring stations. Specifically, the multipath error of BDS rises to 18–37 cm but remains at a relatively low level; the multipath error of GPS increases to 50–55 cm, showing relatively stable performance; in contrast, the multipath error of Galileo fluctuates significantly with a marked increase and ranges from 46 to 101 cm. Overall, BDS maintains the lowest multipath error in both the reference and monitoring station environments, followed by GPS, while Galileo shows the largest and most variable errors.

### 3.3 Monitoring performance evaluation

In this section, we discuss the performance in terms of positioning accuracy and monitoring stability. The positioning performance analysis includes error accuracy and ambiguity fix rate in

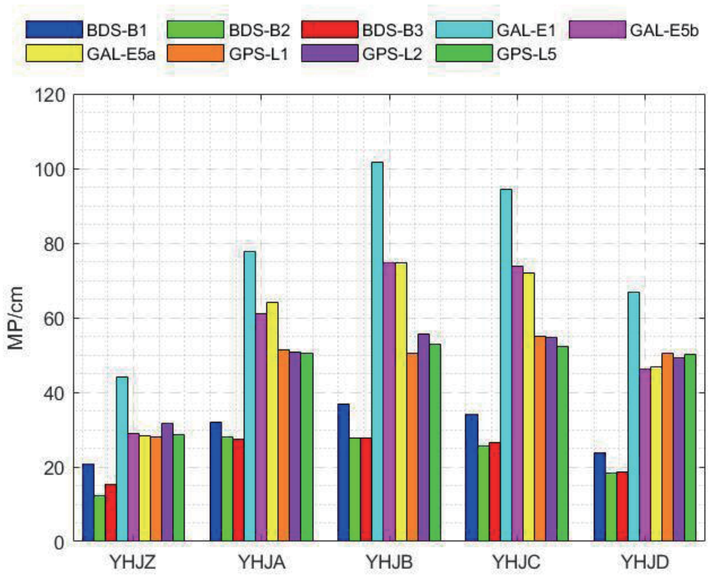


Fig. 8. (Color online) Multipath errors of BDS/Galileo/GPS frequency bands.

the east (E), north (N), and up (U) directions, while the monitoring stability evaluation focuses on the error accuracy of lateral, longitudinal, and vertical displacements.

### 3.3.1 Positioning performance analysis

To explore whether multifrequency data can improve the positioning performance in large-scale transmission infrastructure deformation monitoring compared with dual-frequency data, we selected the YHJA station for analysis. Figure 9 shows the time series of positioning errors for the first 2000 epochs for dual-frequency and triple-frequency solutions for BDS, Galileo, and GPS at the YHJA station. As shown in the figure, the three-frequency solution for BDS outperforms the dual-frequency solution with smoother curves and smaller fluctuations, demonstrating higher accuracy and stability. The three-frequency solution for Galileo shows slight improvements over the dual-frequency solution, but the accuracy enhancement is limited, with both dual-frequency and three-frequency positioning accuracies remaining at the centimeter level. In comparison, the three-frequency solution for GPS significantly outperforms the dual-frequency solution across all directions, with much smaller curve fluctuations and a substantial improvement in both accuracy and stability. Overall, the three-frequency solution shows particularly marked improvements in positioning performance for BDS and GPS, with fluctuation ranges within millimeter-level accuracy, whereas Galileo's improvement is more limited, with fluctuation ranges remaining at centimeter-level accuracy. The significant enhancement seen in BDS and GPS highlights the advantages of using multifrequency data for deformation monitoring in large-scale transmission infrastructure.

Table 2 further shows the average positioning deviation RMS in the E, N, and U directions for dual-frequency and triple-frequency BDS, GPS, and Galileo. As shown in the table, for BDS, the RMS values in the dual-frequency mode are 3.87, 3.91, and 5.57 mm for the E, N, and U

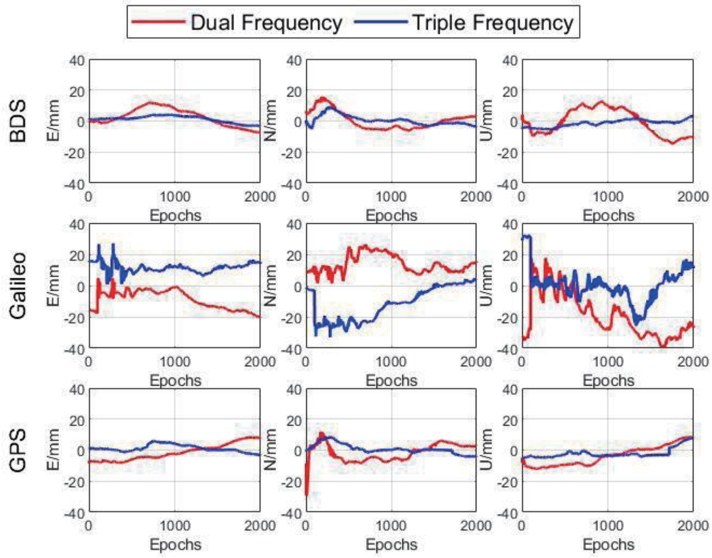


Fig. 9. (Color online) Time series of positioning errors for the first 2000 epochs at the YHJA station for BDS/Galileo/GPS dual-frequency and triple-frequency solutions.

Table 2
RMS values of positioning deviation for BDS, GPS, and Galileo (dual and triple frequencies) at four stations (24 h).

| System | Frequency | Position Bias (unit: mm) | | |
|---|---|---|---|---|
| | | E | N | U |
| BDS | B1/B2 | 3.87 | 3.91 | 5.57 |
| | B1/B2/B3 | 2.24 | 2.17 | 3.52 |
| Galileo | E1/E5b | 12.08 | 12.87 | 15.56 |
| | E1/E5b/E5a | 10.58 | 11.81 | 12.54 |
| GPS | L1/L2 | 3.95 | 4.12 | 5.78 |
| | L1/L2/L5 | 2.25 | 2.33 | 3.63 |

directions, respectively. These values decrease to 2.24, 2.17, and 3.52 mm in the triple-frequency mode, which are improvements of 40.57, 44.5, and 36.8%, respectively. In the GPS dual-frequency mode, the RMS values for the E, N, and U directions are 3.95, 4.12, and 5.78 mm, respectively. In the triple-frequency mode, they decrease to 2.24, 2.33, and 3.63 mm, with improvements of 43.29, 43.45, and 37.2%, respectively, which are comparable to BDS performance. In contrast, the performance improvement for the Galileo system is more limited. In the dual-frequency mode, the RMS values for the E, N, and U directions are 12.08, 12.87, and 15.56 mm, respectively. In the triple-frequency mode, these values decrease to 10.58, 11.81, and 12.54 mm, with improvements of only 12.4, 8.2, and 19.4%, respectively. While there is some improvement in the triple-frequency mode, the positioning accuracy remains in the centimeter range. For the deformation monitoring of large-scale transmission infrastructure, the horizontal accuracy requirement is ±3 mm + 1 ppm and the vertical accuracy requirement is ±5 mm + 1 ppm. Both BDS and GPS triple-frequency solutions meet these requirements.

Figure 10 shows the ambiguity fix rates for BDS, Galileo, and GPS systems in the dual-frequency and triple-frequency modes. As shown in the figure, BDS-2 achieves the highest ambiguity fix rate of 92.2% in the dual-frequency combination (B1/B2), which improves to

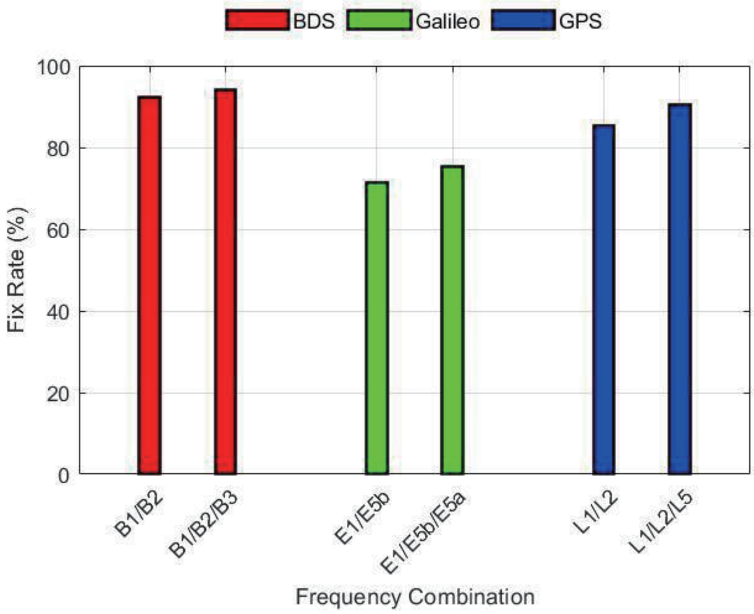


Fig. 10. (Color online) Average ambiguity fix rates for BDS/Galileo/GPS dual and triple frequencies at four stations.

94.1% in the triple-frequency combination (B1/B2/B3), demonstrating excellent fixing performance. GPS follows, with an ambiguity fix rate of 85.4% in the dual-frequency combination (L1/L2), which increases to 90.4% in the triple-frequency combination (L1/L2/L5), showing a significant enhancement in fixing ability. In contrast, Galileo exhibits a lower fix rate, with 71.5% in the dual-frequency combination (E1/E5b), which shows a limited improvement to 75.4% in the triple-frequency combination (E1/E5b/E5a). Overall, the triple-frequency mode shows improvements over the dual-frequency mode in all systems, with BDS and GPS demonstrating particularly strong fixing performance in the triple-frequency mode, while Galileo's fix rate remains relatively low.

The results above show that the triple-frequency mode of BDS and GPS meets the requirements for positioning accuracy and ambiguity fix rate in large-scale transmission infrastructure deformation monitoring. The RMS values for positioning errors in the E, N, and U directions for both systems are within the millimeter range, satisfying the accuracy requirements for horizontal (±3 mm + 1 ppm) and vertical (±5 mm + 1 ppm) displacements. Additionally, the ambiguity fix rates in the triple-frequency mode reach 94.1 and 90.4%, demonstrating high solving accuracy and stability.

### 3.3.2 Monitoring stability analysis

On the basis of the results of the previous positioning performance analysis, we selected the triple-frequency data of GPS and BDS as the subjects for further monitoring stability analysis.

Figures 11 and 12 show the lateral, longitudinal, and vertical displacements for the four monitoring stations of BDS and GPS over three consecutive days. As seen in the figures, the

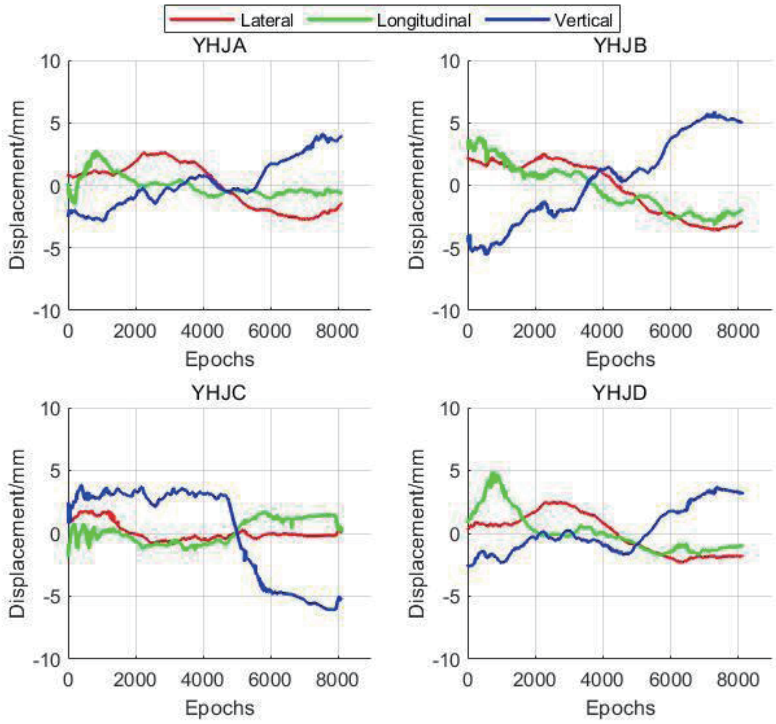


Fig. 11. (Color online) Time series of BDS displacements at four stations over three days.

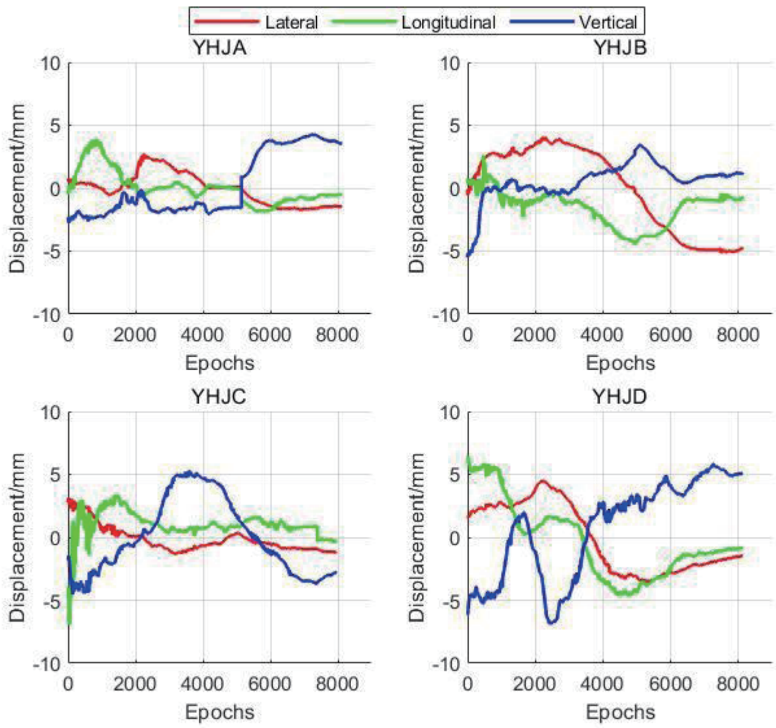


Fig. 12. (Color online) Time series of GPS displacements at four stations over three days.

Table 3
RMS values (mm) of BDS/GPS triple frequency in lateral, longitudinal, and vertical directions over three days.

| System | Monitoring station | Lateral | Longitudinal | Vertical |
|---|---|---|---|---|
| BDS | YHJA | 2.11 | 2.3 | 3.64 |
| | YHJB | 2.34 | 2.24 | 3.28 |
| | YHJC | 2.01 | 2.06 | 3.59 |
| | YHJD | 2.15 | 1.9 | 2.98 |
| GPS | YHJA | 2.13 | 2.28 | 3.49 |
| | YHJB | 2.04 | 2.53 | 3.2 |
| | YHJC | 2.35 | 2.67 | 3.87 |
| | YHJD | 2.33 | 2.28 | 3.25 |

lateral and longitudinal displacements for all four BDS stations fluctuate within the range of [−5, 5] mm, while the vertical displacements range from [−6, 6] mm. For GPS, the lateral and longitudinal displacements for all four monitoring stations fluctuate within the range of [−5, 5] mm, while the vertical displacements fluctuate between [−7, 7] mm. The triple-frequency observations of both systems demonstrate stable performance. Table 3 further shows the RMS values for lateral, longitudinal, and vertical directions from BDS and GPS triple-frequency data over three consecutive days. The positioning accuracies for both BDS and GPS in the lateral and longitudinal directions for all four monitoring stations are higher than 3 mm, and the vertical positioning accuracies are higher than 4 mm. This analysis indicates that, over multiple days of continuous monitoring, the triple-frequency observations of both BDS and GPS remain stable and consistent, meeting the monitoring requirements for large-scale power infrastructure.

## 4. Conclusions

In this study, we explored the application of multifrequency GNSS observations in the deformation monitoring of large-scale power infrastructure in complex electromagnetic environments. Through the analysis of experimental data, the following conclusions were drawn:

Data Quality Analysis: The results of an in-depth analysis of the data completeness rate, *SNR*, *CSR*, and multipath errors showed that BDS exhibits high signal stability in complex electromagnetic interference environments. GPS follows closely, with overall data quality meeting the required standards. However, Galileo demonstrates relatively low data quality, likely owing to fewer satellites received in the Asia-Pacific region and higher levels of electromagnetic interference.

Positioning Accuracy Analysis: In the deformation monitoring of large-scale power infrastructure, the multifrequency GNSS positioning accuracy was significantly higher than that in the dual-frequency mode. The BDS triple-frequency solution showed improvements of 40.57, 44.5, and 36.8% in the E, N, and U directions, respectively, compared with the dual-frequency mode. GPS showed improvements of 43.29, 43.45, and 37.2% in the same directions. Both BDS and GPS triple-frequency solutions meet the accuracy requirements of ±3 mm in the E and N directions, and ±5 mm in the U direction, with ambiguity fix rates exceeding 90%. These results demonstrated that they meet the deformation monitoring requirements for large-scale power infrastructure. The sensor capabilities of GNSS receivers are pivotal in achieving these high levels of accuracy, as they enable precise measurements of deformation in the infrastructure. In contrast, Galileo performs poorly in both dual-frequency and triple-frequency modes, failing to meet the monitoring requirements.

Monitoring Stability Analysis: Multifrequency GNSS observations demonstrated excellent stability in long-term monitoring. BDS and GPS triple-frequency solutions showed extremely high monitoring reliability, with deformation parameters at multiple monitoring stations remaining relatively stable. Their error accuracy in lateral, longitudinal, and vertical displacements meets the requirements for large-scale power infrastructure monitoring.

Multifrequency GNSS observations significantly enhance the accuracy and stability of deformation monitoring in complex environments. However, challenges such as electromagnetic interference and geographic obstructions persist, leaving room for improvement. Future research should focus on the following directions: developing anti-jamming algorithms and data quality optimization strategies tailored to complex electromagnetic environments, integrating GNSS with other monitoring methods to enhance system reliability through multisource data fusion, and applying machine learning to model and predict deformation data, enabling early warnings for the safe operation of large-scale transmission infrastructure. These advancements will further optimize the role of GNSS sensors, improving their effectiveness in complex monitoring scenarios.

## Acknowledgments

This work was supported by the National Natural Science Foundation of China (42404035) and R&D Program of Beijing Municipal Education Commission (KM202410016007).

## References

1 M. Liu, Y. Li, H. Zhang, and C. S. Wang: Electr. Power **45** (2012) 34. https://doi.org/10.3969/j.issn.1004-9649.2012.05.008
2 J. J. Guo and S. J. Ge: Proc. 10th Int. Technical Meeting of the Satellite Division of The Institute of Navigation (ION GPS) (Kansas City, MO, 1997). https://api.semanticscholar.org/CorpusID:114446554
3 D. Egea-Roca, M. Arizabaleta-Diez, T. Pany, F. Antreich, J. A. López-Salcedo, M. Paonni, and G. Seco-Granados: IEEE Access **10** (2022) 39939. https://doi.org/10.1109/ACCESS.2022.3165594
4 W. Guo, G. Wang, Y. Bao, M. Zhang, X. Sun, R. Zhao, and W. Gan: Geomatics Inf. Sci. Wuhan Univ. **45** (2020) 1043. https://doi.org/10.13203/j.whugis20190015
5 J. W. Lovse, W. F. Teskey, G. Lachapelle, and M. E. Cannon: J. Surv. Eng. **121** (1995) 35. https://doi.org/10.1061/(ASCE)0733-9453(1995)121:1(35)
6 P. Breuer, T. Chmielewski, P. Górski, and E. Konopka: Wind Struct. **5** (2002) 419. https://api.semanticscholar.org/CorpusID:110788080
7 J. Guo, L. Xu, L. Dai, M. McDonald, J. Wu, and Y. Li: J. Bridge Eng. **10** (2005) 163. https://doi.org/10.1061/(ASCE)1084-0702(2005)10:2(163)
8 W. Dai, J. Zhu, X. Ding, and Y. Chen: Geomatics Inf. Sci. Wuhan Univ. **32** (2007) 234. https://doi.org/10.3969/j.issn.1671-8860.2007.03.012
9 J. R. Vázquez-Ontiveros, C. A. Martínez-Felix, G. E. Vázquez-Becerra, J. R. Gaxiola-Camacho, A. Melgarejo-Morales, and J. Padilla-Velazco: Adv. Space Res. **69** (2021) 319. https://doi.org/10.1016/j.asr.2021.09.018
10 N. Shen, L. Chen, X. Lu, Y. Ruan, H. Hu, Z. Zhang, L. Wang, and R. Chen: GPS Solut. **26** (2022) 48. https://doi.org/10.1007/s10291-021-01215-x

11 M. Guan, L. Yin, M. Duan, T. Zhang, J. Liu, and Y. Zhang: Automation Technol. Appl. (n.d.). https://link.cnki.net/urlid/23.1474.tp.20241125.1559.027
12 J. Bu, K. Yu, N. Qian, X. Zuo, and J. Chang: IEEE Access **9** (2021) 5845. https://doi.org/10.1109/ACCESS.2020.3048352.
13 Y. Liu: Jiangxi Surv. Mapp. **3** (2020) 12.
14 C. Yang: Surv. Mapp. Spatial Geogr. Inf. **45** (2022) 139. https://doi.org/10.3969/j.issn.1672-5867.2022.09.040
15 L. Zhang: Surv. Mapp. Spatial Geogr. Inf. **46** (2023) 87.
16 C. He, Z. Wang, and T. Zhang: Global Positioning Syst. **49** (2024) 120. https://doi.org/10.12265/j.gnss.202318
17 China Standards Press. China Earthquake Administration: Specifications for the construction of seismic stations: Global Navigation Satellite System Reference Stations (DB/T 19-2020) (China Standards Press, Beijing, 2021).
18 X. Zhang and L. Ding: J. Wuhan Univ. Inf. Sci. Ed. **38** (2013) 832.
19 C. Sun, Y. Wang, R. Ding, and J. Zhang: Surv. Mapp. Spatial Geogr. Inf. **46** (2023) 29. https://doi.org/10.3969/j.issn.1672-5867.2023.06.009.
20 W. Jiao and L. Bi: J. Civil Avi. Univ. China **36** (2018) 1. https://doi.org/10.3969/j.issn.1674-5590.2018.01.001
21 Z. Zhang, C. Lin, K. Gao, and B. Zhao: Beijing Surv. Mapp. **36** (2022) 517. https://doi.org/10.19580/j.cnki.1007-3000.2022.04.027
22 Y. Guo, Y. Zhang, J. Ren, and J. Wang: North China Earthquake Sci. **39** (2021) 58. https://doi.org/10.3969/j.issn.1003-1375.2021.03.009
23 Q. Zhang, L. Zhang, A. Sun, X. Meng, D. Zhao, and C. Hancock: Remote Sens. **16** (2024) 189. https://doi.org/10.3390/rs16010189
24 Y. He: Railway Surv. and Mapp. **50** (2024) 13. https://doi.org/10.19630/j.cnki.tdkc.202405210001
25 T. Liu and B. Zhang: J. Geodesy **95** (2021) 97. https://doi.org/10.1007/s00190-021-01549-x
26 G. Li, J. Wu, C. Zhao, and Y. Tian: GPS Solut. **21** (2017) 1161. https://doi.org/10.1007/s10291-017-0599-4
27 K. Stępniak, O. Bock, P. Bosser, and P. Wielgosz: GPS Solut. **26** (2022) 74. https://doi.org/10.1007/s10291-022-01261-z
28 K. C. T. Swamy, D. V. Ratnam, T. Suman, and S. T. Ahmed: Measurement **207** (2022) 112385. https://doi.org/10.1016/j.measurement.2022.112385
29 Y. Gao and X. Shen: Navigation **49** (2002) 109. https://doi.org/10.1002/j.2161-4296.2002.tb00260.x
30 S. Bian, Y. Liu, B. Ji, and W. Zhou: J. Wuhan Univ. Inf. Sci. Ed. **49** (2024) 21. https://doi.org/10.13203/j.whugis20220021
31 D. Yang, C. Tan, F. Wang, and T. Li: J. Electron. Inf. Technol. **46** (2024) 1373. https://doi.org/10.11999/JEIT230462
32 Q. Cai, F. Zhu, X. Chen, and L. Ma: GNSS World China **48** (2023) 24. https://doi.org/10.12265/j.gnss.2022070


## About the Authors

**Jiaxing Wang** is currently a graduate student at Beijing University of Civil Engineering and Architecture, China. His current research interests are in precise point positioning and deformation monitoring.

**Gen Liu** received his Ph.D. degree from Wuhan University, China, in 2019. He is currently an associate professor at Beijing University of Civil Engineering and Architecture, China. His research interests are in precise point positioning and multisensor fusion positioning technology.

**Haochen Guo** is currently a graduate student at Beijing University of Civil Engineering and Architecture, China. His current research interests are in precise point positioning and correcting tropospheric delay errors.

**Nanjun Ma** is currently studying at Beijing University of Civil Engineering and Architecture, China. His research focuses on precise point positioning and GNSS deformation monitoring.

**Jian Wang** received his Ph.D. degree from China University of Mining and Technology, China, in 2006. He is currently a professor at Beijing University of Civil Engineering and Architecture, China. His current research interests are in precise GNSS positioning, GPS/inertial and other sensor integrations, indoor and personal navigation, visual SLAM, and mining disaster monitoring.